Available online at www.sciencedirect.com
ScienceDirect
Trans. Nonferrous Met. Soc. China 29(2019) 473−484
Transactions of Nonferrous Metals Society of China
www.tnmsc.cn

Effect of electromagnetic interaction on microstructure and corrosion resistance of 7075 aluminium alloy during modified indirect electric arc welding process

J. S. REYNA-MONTOYA[1], M. A. GARCÍA-RENTERÍA[1], V. L. CRUZ-HERNÁNDEZ[2], F. F. CURIEL-LÓPEZ[1], L. R. DZIB-PÉREZ[3], L. A. FALCÓN-FRANCO[1]

1. Faculty of Metallurgy, Autonomous University of Coahuila, Carretera 57 Km. 5 CP 25720, Monclova, Coahuila, México;
2. Instituto de Investigación en Metalurgia y Materiales, Universidad Michoacana de San Nicolás de Hidalgo, A. P. 888, CP 58030, Morelia, Michoacán, México;
3. Centre for Corrosion Research, Autonomous University of Campeche, Av. Agustín Melgar s/n, Col. Buenavista, CP 24039, Campeche, Cam, México

Received 28 April 2018; accepted 9 July 2018

Abstract: The effects of applying an electromagnetic interaction of low intensity (EMILI) on the microstructure and corrosion resistance of 7075-T651 Al alloy plates (13 mm in thickness) during modified indirect electric arc (MIEA) welding were investigated. The welding process was conducted in a single pass with a heat input of ~1.5 kJ/mm. The microstructural observations of the welds were correlated with the effect of EMILI on the local mechanical properties and the corrosion resistance in natural seawater by means of microhardness measurements and electrochemical impedance spectroscopy, respectively. Microstructural characterization of the welds revealed a grain refinement in the weld metal due to the electromagnetic stirring induced by EMILI of 3 mT during welding. In addition, observations in the scanning electron microscope showed that the precipitation of Cu-rich phases and segregation of eutectics were reduced in the heat affected zone (HAZ) also as an effect of EMILI. The high corrosion dissolution of the 7075-T651 welds in natural seawater and the extent of overaging in the HAZ were reduced when welding with EMILI of 3 mT. Thus, EMILI along with the MIEA technique may lead to welded joints with better microstructural characteristics, improved mechanical properties in the HAZ and reduced electrochemical activity.

Key words: 7075-T651 Al alloy; modified indirect arc welding; microstructural characterization; corrosion resistance; electromagnetic interaction

1 Introduction

Aluminium alloys (AA) are versatile materials used for common and specific applications due to the possibility of manufacturing components with diverse metals and non-metals in order to improve the mechanical properties preserving a high specific strength ratio. The excellent characteristics such as specific strength ratio and good capacity of deformation of Al−Zn−Mg alloys make these alloys very attractive material in structural, metal mechanics applications, transportation and aeronautical industries [1]. The attractive properties of these AA, 7xxx series, are due to the formation of intermetallic phases through the well-known precipitation sequence: supersaturated solid solution (SSSS) → Guiner−Preston (GP) zones → semi-coherent precipitates $MgZn_2$ (η') → non-coherent precipitates $MgZn_2$ (η) → non-coherent precipitates $Mg_3Zn_3Al_{12}$ (T) [2,3]. The semi-coherent GP zones and η'-phase provide hardening reinforce to the α-matrix [4,5]. For instance, diverse components for aeronautical applications and transportation industry require to be joined by different bonding methods such as rivets, adhesives and screws. In some structural applications, it is necessary to use fusion welding processes, where heat input from the welding thermal cycle promotes microstructural transformation that reduces the mechanical and chemical characteristics of the AA welded joints [6]. The main problem in fusion

Corresponding author: M. A. GARCÍA-RENTERÍA; E-mail: marcogarciarenteria@uadec.edu.mx
DOI: 10.1016/S1003-6326(19)64956-3

welding of Al alloys is the porosity formation within the weld metal (WM), due to the high solubility of hydrogen at high temperature in molten condition [6−8]. Porosity is a defect frequently found in the weld pool of fusion welded AA which can reduce the mechanical properties of the welded joints [9−11]. Additionally, several problems are encountered in heat treatable AA welds in the heat affected zone (HAZ) due to the segregation of solute-rich liquid at grain boundaries near the fusion line in the partial molten zone (PMZ) [12], promoting hot cracking [13−19]. Moreover, in 7xxx series AA, fusion welds present softening in the HAZ associated to the overaging phenomenon due to the precipitation and growth of the η phase. This effect takes place for the transformation $\eta' \rightarrow \eta$ in the temperatures range from 230 to 350 °C during hot deformation [20]. Also, the dissolution of η' phase and the growth of η phase can take place in the temperature range from 350 to 380 °C easily attained during the welding thermal cycle [21−23].

Many AAs exhibit improved mechanical strength, but they result in an increase of the susceptibility to corrosion degradation due to the precipitation of coherent and semi-coherent phases and coarse second phase particles [24]. Commercial-grade AAs, such as 7075, contain numerous constituent particles of various sizes, which have electrochemical potentials different from those of the surrounding matrices rising the electrochemical activity in the metal matrix [25−27]. The presence of intermetallic strengthening precipitates creates discontinuities on the passive corrosion product film and makes them susceptible to stress corrosion cracking [28]. Besides, the precipitates can induce the formation of localized anode sites on the surface, whereas the aluminium matrix remains passive, resulting in pitting or crevice corrosion. Pitting corrosion is one of the most insidious and dangerous forms of localized corrosion in passive alloys, because minimal metal mass loss is involved from very small areas associated with depth penetration to the bulk of the component which can lead to the failure of the entire engineering component or structure [29].

The acceptable corrosion resistance of AA in a broad variety of environments is due to the formation of the stable and protective passive oxide (Al_2O_3) layer that inhibits further oxidation of the underlying AA which is thermodynamically reactive. The passive film becomes unstable and degrades locally by appearance of flaws and discontinuities that promote the local dissolution, causing film breakdown and localized corrosion [29,30]. In the case of welds of AA 7xxx series, artificial aging and retrogression re-aging heat treatments can improve the corrosion resistance of 7075 AA notwithstanding the discontinuous distribution of η precipitates at the grain boundaries [31]. During welding of 7075 AA, the growth and coalescence of precipitates in the HAZ induce anodic behavior of this zone compared with weld metal and base metal [32,33]. However, post weld heat treatment can improve localized corrosion resistance because of the redistribution of reinforcing precipitates in HAZ [34].

For decades, the subject of joining AA for fusion welding processes and the adverse effects induced in the microstructure has been studied and reported by several research groups [6,35]; however, limited improvements have been accomplished and the use of solid state welding process can be a valuable option as some defects are reduced [36,37]. One method developed in recent years is the modified indirect electric arc (MIEA). This method is proved to improve the microstructural evolution during welding, maintain an acceptable level of the mechanical properties in both the welding pool and the HAZ, and also enhance the resistance to fatigue life [38]. Moreover, there is a lack of information about the influence of external driving forces such as electromagnetic interaction of low intensity (EMILI) applied during welding. The EMILI can induce grain refinement of the weld metal, thus improving the mechanical properties [39−41]. Recently, some researches refer to the improvement on weld quality of dissimilar welds of Al to other materials [42−44], but there are not reports about the combined effect of the MIEA and electromagnetic stirring (EMS) on the microstructural evolution during welding and the improved mechanical properties and corrosion resistance. In this instance, an experimental set-up was implemented for welding real service plates of 7075-T651 AA using the MIEA under the effect of EMILI as a first assessment before welding dissimilar metals. In the present work, welded joints of the 7075-T651 AA (13 mm in thickness) were conducted in a single pass avoiding the multi-pass process to minimize the deterioration on the corrosion resistance and the mechanical properties. Thus, the objective of this work was to evaluate the influence of MIEA and EMILI on the microstructural evolution of the 7075-T651 AA during welding and their effect on the mechanical properties and surface properties in terms of corrosion resistance in natural seawater.

2 Experimental

2.1 Materials and welding processes

Plates of 7075-T651 Al alloy (12.7 mm × 90 mm × 150 mm) were GMA-welded with the MIEA process using as filler metal an electrode ER-5356 of 1.2 mm in diameter. Table 1 shows the chemical composition of base metal (BM) and filler metal.

Welding set-up is shown in Fig. 1(a) and welding

joint preparation configuration corresponding to the MIEA proposed by AMBRIZ et al [38] for 6061-T6 Al alloy is shown in Fig. 1(b). Plates were mechanically cleaned, degreased and preheated at 80 °C before weld beads were deposited in a single pass with a semiautomatic GMAW process and direct current positive electrode (DC-PE), with the operative variables shown in Table 2 with a heat input ~1.5 kJ/mm. The shielding gas used was Ar flowing at 20 L/min and the filler metal was fed at 190 mm/s with a welding speed of 3.6 mm/s and stick-out of 10 mm. External EMILI was induced with a variable current power supply feeding a coil around welding set up as shown in Fig. 1(a). The magnetic flow density was measured with a Gaussmeter to control and apply intensities of 0, 3 and 12 mT, based on the experiments at magnetic field intensities of 3 and 12 mT on previous observations [41].

2.2 Microstructural characterization

Microstructural characterization was focused on a quantitative analysis of the main areas, grain size, chemical composition and distribution of precipitates and their structures by optical, scanning electron and transmission electron microscopy, respectively.

The microstructures of 7075-T651 plates in the as-received condition and samples taken from transverse sections of the welded joints were characterized. Previous to metallographic examination, samples were ground with SiC emery paper (220, 400, 600, 1200 and 2000 grit). The samples were subjected to polishing to a mirror-like surface finish using diamond past of 6, 3 and 1 μm and finally were electropolished with a solution of 20 mL $HClO_4$ + 100 mL C_2H_6O using a graphite bar as cathode and applying 10 V during 6 s. The samples were chemically etched by immersion in a Keller reagent (75 mL HCl + 25 mL HNO_3 + 5 mL HF + 25 mL H_2O) for 2 s. This metallographic preparation was used for revealing the actual configuration profile on the cross-section of the samples, where it was possible to identify the HAZ, segregation zone (SZ) and fusion zone (FZ). The amount of base metal diluted (BMD) in FZ (η) was measured using a modified version of Lippold equation (Eq. (1)) [45], with data acquired from welded samples, where A and B correspond to the amounts of the BMD and A+B+C is the total amount of BMD in FZ, as shown in Fig. 2.

$$\eta = \frac{A+B}{A+B+C} \times 100\% \quad (1)$$

Metallographic analysis of the BM and welded samples was made in digital micrographs obtained by optical microscopy (OM) and measured with the help of a software. Measurements were conducted in terms of the grain size. In order to determine the chemical compositions of different phases and segregation present in the HAZ and SZ of the samples, the welds were analyzed in a field emission scanning electron microscope (FE-SEM) equipped with and energy dispersive X-ray (EDX) analyzer.

Table 1 Chemical compositions of base metal and filler metal (wt.%)

Material	Al	Zn	Mg	Cu	Si	Ti	Mn	Fe
BM 7075	88.6	6.4	2.7	1.7	0.03	0.02	0.02	0.19
Filler wire ER-5356	93.44	0.10	5.5	0.10	0.25	0.06	0.20	0.35

Table 2 Welding parameters

Magnetic field intensity/mT	Current/A	Voltage/V	Electrode feeding rate/(mm·s^{-1})	Stick-out/mm	Welding speed/(mm·s^{-1})
0	275	26	190	9	3.6
3	240	26	190	9	3.6
12	260	25	190	9	3.6

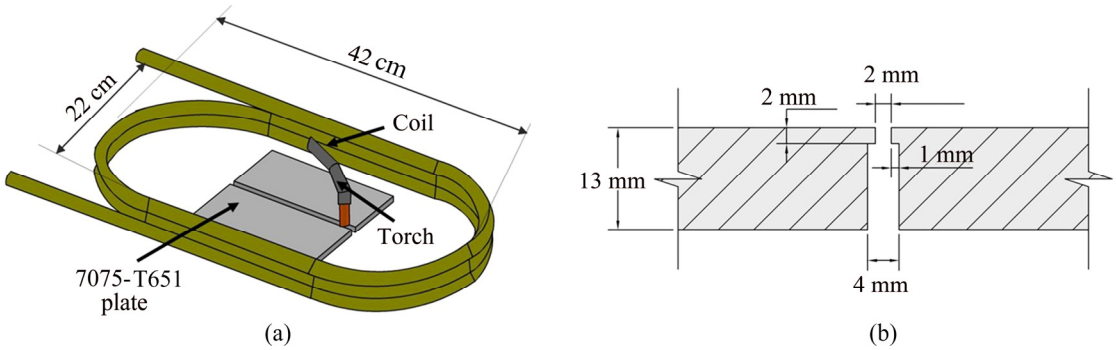

Fig. 1 Experimental set-up (a) and MIEA welding grove configuration (b)

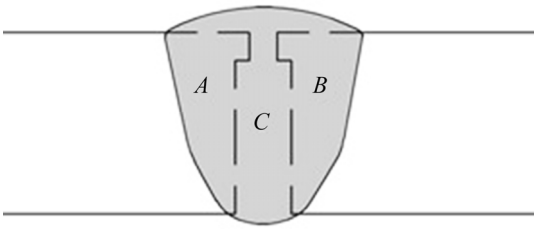

Fig. 2 Weld profile measurements modified from Ref. [45]

X-ray diffraction analysis was applied to samples of BM and welded joints in order to determine type of phases with a diffractometer using monochromatic Cu K_α radiation (λ=0.1542 nm), a step size of 0.02° and a time step of 0.6 s. For transmission electron microscopy (TEM) characterization, thin foils of 3 mm in diameter and 0.5 mm in thickness, were cut from the HAZ and SZ of the samples as shown in Fig. 3. The samples were thinned to 30−40 μm with SiC emery paper and subjected to electropolishing with a double-jet machine using an electrolytic solution of 25 vol.% HNO_3 + 75 vol.% C_2H_6O at −25 °C, applying a current of 20 mA and a voltage of 20 V. For bright field TEM (BFTEM) and high resolution TEM (HR-TEM) techniques were used in a TEM operating at 200 kV.

Fig. 3 Section for TEM analysis in HAZ of welded joints

2.3 Vickers microhardness test

Vickers microhardness (HV) tests were conducted in samples taken from the welded joints and compared with the BM for microhardness test in order to determine changes on the local mechanical properties. The preparation of samples was similar to that used for metallographic analysis. Vickers microhardness profiles were generated by applying a load of 100 g ($HV_{0.1}$) during 15 s. Results were plotted according to the virtual mesh shown in Fig. 4 to generate a map of the microhardness profile in different regions of the welded joints.

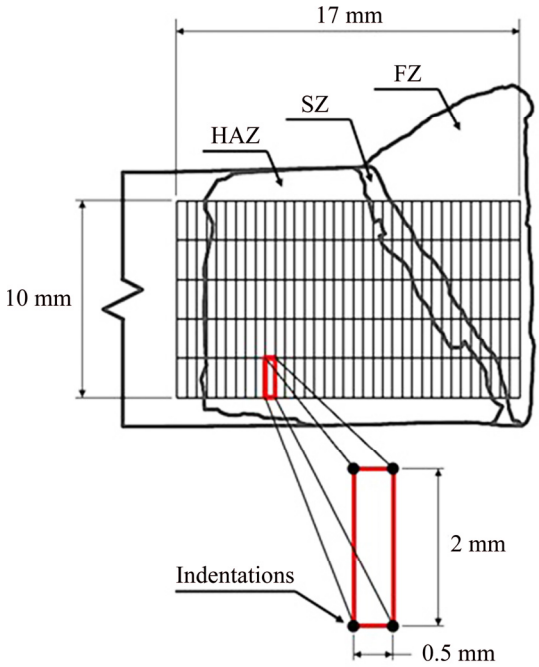

Fig. 4 Definition of virtual mesh for microhardness ($HV_{0.1}$) indentations on cross-section of weld zone

2.4 Evaluation of corrosion resistance

The effect of EMILI during welding on the corrosion resistance of the welded samples was evaluated by means of electrochemical impedance spectroscopy (EIS) and compared with samples of BM in the as-received condition. The studied samples (1 cm^2), obtained from welded plates of similar position, were embedded in epoxy resin and connected with copper wire in the rear. Electrochemical measurements were conducted using an electrochemical work station controlled by Zcorr® software and connected to a conventional three-electrode electrochemical cell open to the air. The working electrodes were the BM and welded samples, a saturated calomel electrode (SCE) was used as reference electrode and a graphite rod as auxiliary electrode.

Before all experiments, the potential was stabilized at free potential during 30 min, the impedance measurements were then carried out. EIS tests were realized at open circuit potential (OCP) in the frequency range of 20 kHz to 50 mHz at an AC amplitude of 15 mV. All tests were performed in non-deaired natural seawater at room temperature of (26±1) °C. Seawater physicochemical parameters are shown in Table 3.

3 Results

3.1 Macro and microstructural characterization

Figure 5 shows the cross-section profiles of welded joints from which the main areas involved in microstructural changes are measured after Keller's

Table 3 Physicochemical parameters and chemical compositions of seawater

Salinity/%	pH	Concentration of dissolved O_2/(mg·L^{-1})	Conductivity/ (mS·cm^{-1})	Composition/(g·kg^{-1})						
				Cl^-	Na^+	K^+	SO_4^{2-}	HCO_3^-	Ca^{2+}	Mg^{2+}
36	8.2	6.8	50.8	19.35	10.77	0.39	2.71	0.14	0.41	1.29

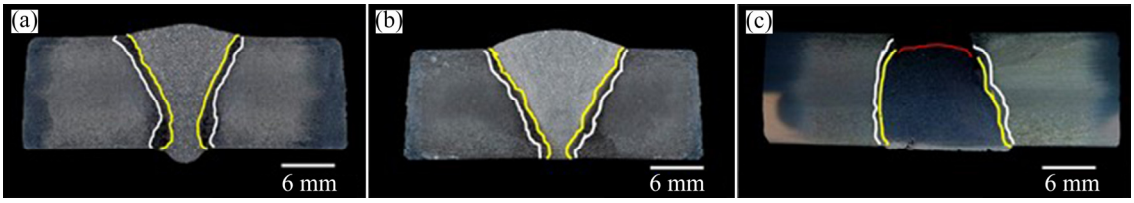

Fig. 5 Cross-section profiles of welded samples: (a) 0 mT; (b) 3 mT; (c) 12 mT

chemical etching. Table 4 shows the data obtained from the analysis of the FZ, SZ and HAZ of the welded joints. The OM images in Fig. 5 show that the weld profiles changes when EMILI is induced by the application of a magnetic field of 3 mT which increases the FZ due to larger quantity of melt BM. Nevertheless, samples welded at 12 mT show an excess of melt BM and the final weld is unacceptable because excessive penetration. Additionally, a reduction of HAZ on the welded joints can be seen when EMILI is induced during welding by application of both 3 and 12 mT.

Table 4 Area quantification of welded joints in main welding cycle thermal-affected regions

Magnetic field intensity/mT	Area/mm^2		
	FZ	SZ	HAZ
0	98.84	33.93	302.10
3	150.14	33.77	281.74
12	92.64	31.14	268.40

The grain structures of different regions in welded joints obtained from optical micrograph analysis are shown in Fig. 6. From these optical micrographs, the grain refinement of the SZ is clearly observed with respect to FZ and HAZ. The grain refinement in the SZ is attributable to the recrystallization phenomena promoted by the peak temperature attained during welding thermal cycle. This effect is related to the partially melted BM which promotes the segregation of low temperature alloying elements at grain boundaries [18,19].

Welds made with EMILI at 3 mT presented a smaller grain size as shown in Fig. 6(d), than welds made without EMILI and with application of 12 mT in FZ as revealed in Figs. 6(a) and (g), respectively. Moreover, a reduction of the SZ is visible as indicated in Table 4, which means a reduction of intergranular segregation.

Figure 7 shows the cumulative frequency plots acquired from grain size measurements of optical microscopy micrographs. Data intervals for the cumulative frequency were acquired every 5 μm (interval class) up to values >120 μm and presented in the *x*-axis as grain size, the *y*-axis presented the resembled values in cumulative percent by the sum of frequency values depending on grain size. There can be seen that the 90% cumulative grain size corresponds to 95, 80 and 105 μm in the FZ of the 0, 3 and 12 mT welds, respectively, and the mean grain size of the BM corresponds to 85 μm. The grain refinement obtained in FZ was ~20% in welds made with 3 mT and ~13% in welds made with 12 mT when compared with welds made without EMILI.

FE-SEM micrographs of the weld zones of different samples are shown in Fig. 8. Rod- and plate-like precipitates corresponding to the η'-phase $Mg(ZnCuAl)_2$ were found in the HAZ of samples welded with 0 mT and in the SZ of samples welded with 3 mT. However, in the welds made with 12 mT this kind of precipitates were not observed. The *S*′-phase (Al_2CuMg), was found in both FZ and SZ in the HAZ. The presence of the ternary *S*′-phase in FZ is due to the effect of molten BM dragged to the weld pool during welding. *S*′-phase can nucleate and grow during solidification and cooling of weld metal starting as a segregated eutectic. This phase with high Cu content can negatively influence the corrosion resistance of welded joints because it is more electrochemically active than the Al matrix [46].

XRD patterns of the BM and welded samples are shown in Fig. 9. The strongest peaks (111), (200), (220) and (311) correspond to the typical reflections of Al matrix, whereas the main strengthening phase of the 7075 AA, $MgZn_2$, can be observed in the (201) reflection peak in all samples. On the other hand, the corrosion detrimental phases Al_2Cu and Al_7Cu_2Fe are the most predominant phases in both BM and welded samples; nonetheless, there are tenuous (420) and (221) reflection peaks respectively in sample welded with 3 mT. These observations indicate a growth suppression of the Al_2Cu and Al_7Cu_2Fe phases during welding with 3 mT,

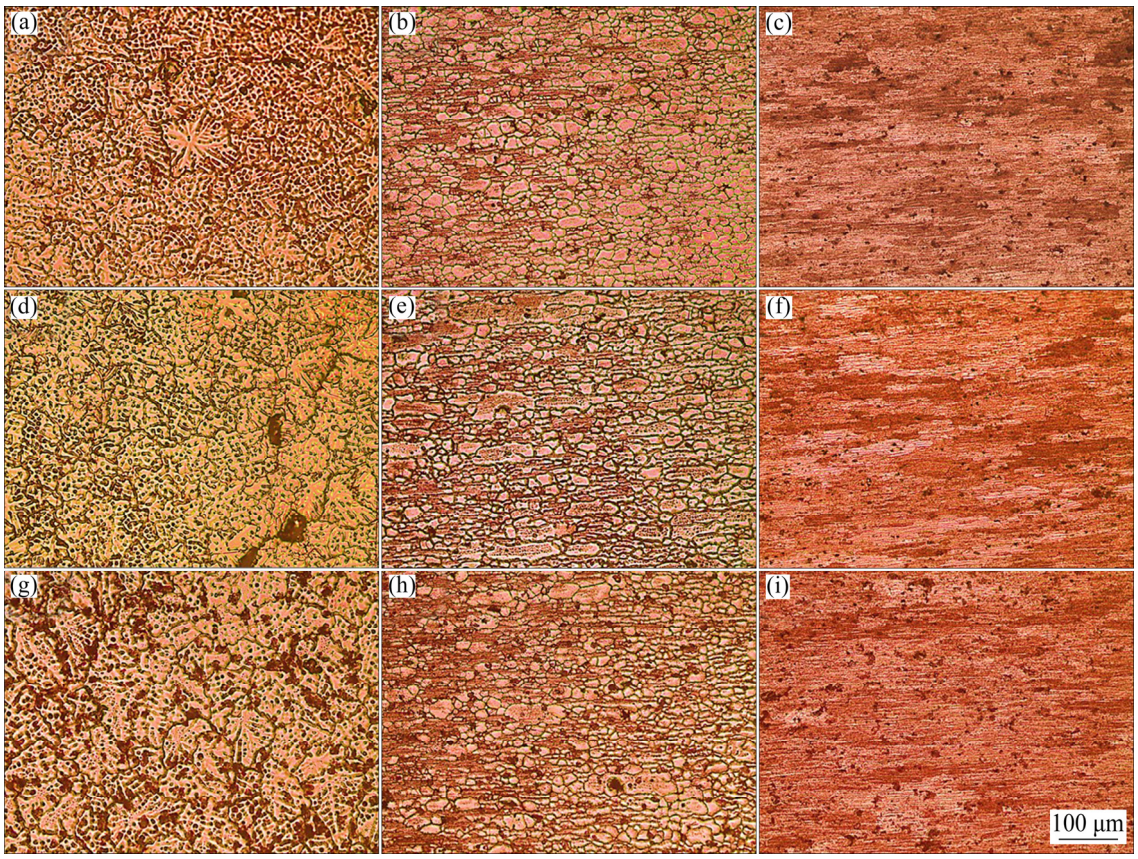

Fig. 6 Representative optical microscopy micrographs of weld zone: (a−c) 0 mT; (d−f) 3 mT; (g−i) 12 mT

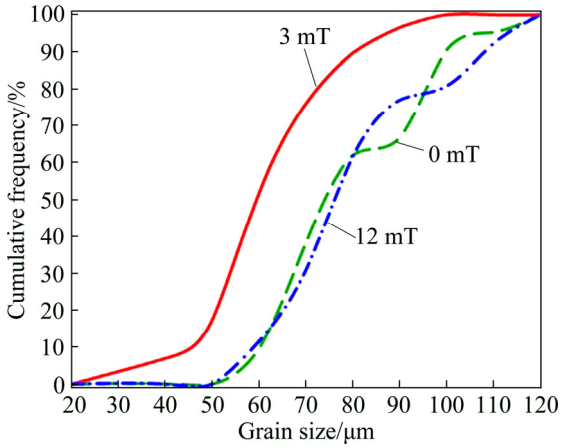

Fig. 7 Cumulative frequency vs grain size in FZ of welded samples

attributable to the magnetic constriction during thermal cycle in solid state of the welded sample due to interaction between external EMILI and the EMF inherent to the welding process.

HAZs of the welds were characterized by high resolution transmission electron microscopy (HR-TEM). The precipitates found in the samples are shown in Fig. 10. Electron diffraction patterns of the samples were indexed with the fast Fourier transform (FFT) using the Digital Micrograph software. In the welds made with 0 and 3 mT, the precipitates of $MgZn_2$ in Figs. 10(a) and (c), presented a closed packed hexagonal structure in the preferential directions $[\bar{1}2\,\bar{1}3]$ and $[01\,\bar{1}0]$ respectively which are non-coherent with Al matrix with preferential orientation [100]. The electron diffraction pattern taken from the HR-TEM image shown in Fig. 10(b) for the weld made with 0 mT shows the hexagonal Al_7Cu_2Fe phase in the preferential direction $[01\,\bar{1}1]$, whereas in weld made with 12 mT in Fig. 10(d), the $Al_{18}Cr_2Mg_3$ phase was found in the $[1\,\bar{1}0]$ direction. These observations correlate well with the reflections indexed in XRD patterns in Fig. 9.

3.2 Local mechanical characterization

In the representation of the microhardness ($HV_{0.1}$) profiles shown in Fig. 11, the weld zone regions are delimited on the hardness maps, which are in good correlation with the microstructural profile. From these microhardness ($HV_{0.1}$) maps, a softening zone can be seen in the HAZ of weld made without EMILI corresponding to values from $HV_{0.1}$ 80 to $HV_{0.1}$ 100; whereas an improvement of this mechanical property of samples welded with EMILI can be appreciated in Fig. 11, where softening regions have microhardness values of $HV_{0.1}$ 140 and $HV_{0.1}$ 120 in samples welded with 3 and 12 mT, respectively. This effect is attributable

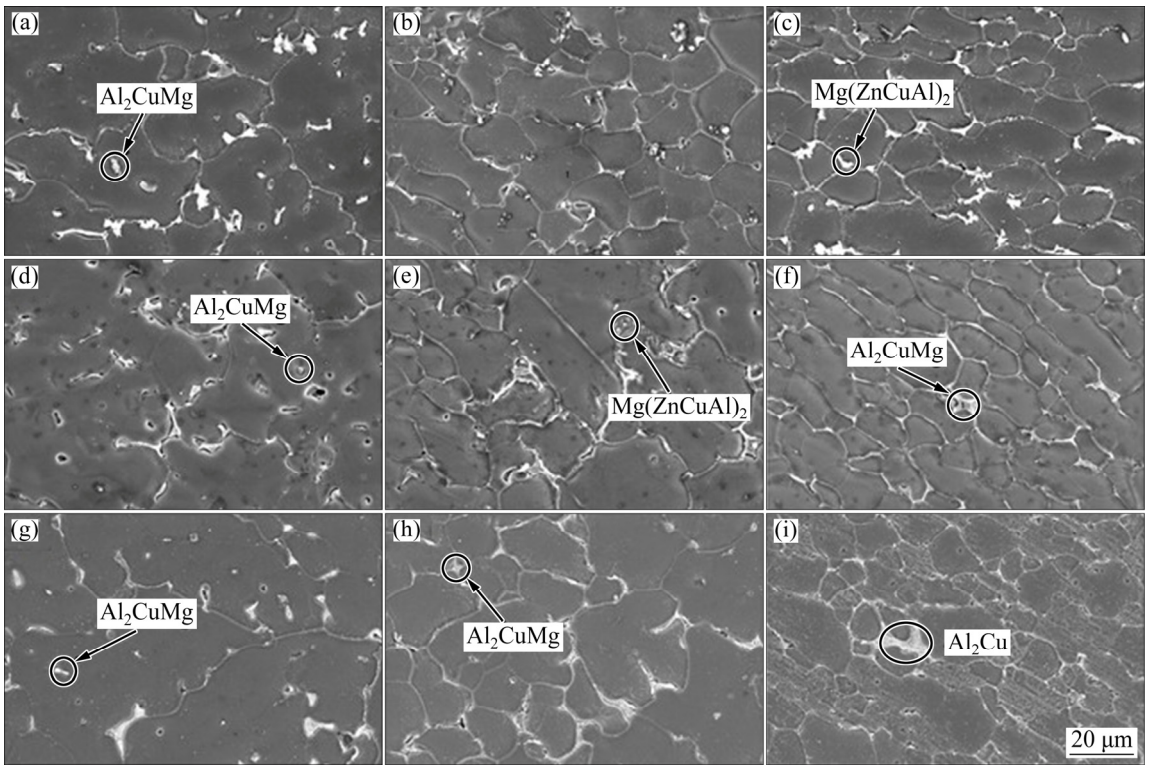

Fig. 8 FE-SEM micrographs showing presence of η' and S' phases in welded zone of samples: (a−c) 0 mT; (d−f) 3 mT; (g−i) 12 mT

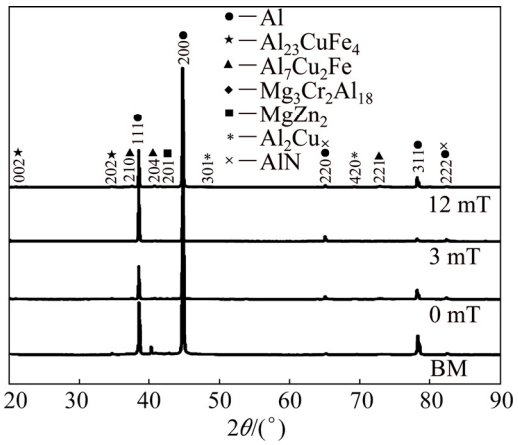

Fig. 9 XRD patterns of BM and welded samples

to the interaction between the inherent EMF generated by the welding process and the external EMILI, which retard the transformation $\eta' \rightarrow \eta$ during welding thermal cycle, similar to that observed in 6063 AA [41].

3.3 Evaluation of corrosion resistance

The results from impedance measurements on 7075-T651 AA samples welded under different conditions in natural seawater are shown in Fig. 12(a) (Nyquist diagram) and (b) (Bode diagram). Figure 12(a) exhibits the same electrochemical behavior: presence of only one capacitive semi-arc. In the Nyquist diagram, it can be seen that the BM presents the biggest capacitive semi-arc. The lower capacitive semi-arc obtained for the welded sample without application of EMILI (0 mT) compared with that obtained for the BM, suggests that the welding process has a negative effect on the corrosion resistance. The results show an improvement on the corrosion resistance (larger capacitive semi-arc) for welded samples under the influence of electromagnetic field of 3 mT with respect to welded samples without application of electromagnetic field (0 mT), as well as a decrease on the corrosion resistance (lower capacitive semi-arc) for welded samples under the influence of magnetic field of 12 mT.

In the Bode magnitude diagram (Fig. 12(b)), the higher impedance of 7.0 $k\Omega \cdot cm^2$ was obtained for BM compared with the welded samples with 0 (3.1 $k\Omega \cdot cm^2$), 3 (3.5 $k\Omega \cdot cm^2$) and 12 mT (2.6 $k\Omega \cdot cm^2$). These values are in agreement with previous results from Nyquist diagram. In Bode phase angle, maximum values are observed close to 90°, characteristic values of a capacitive behavior.

These results indicate that the detrimental effect of the welding process was not significantly annulled with the simultaneous application of EMILI; nonetheless, it was reduced with the EMILI of 3 mT in comparison with 0 and 12 mT.

Different equivalent electric circuits have been reported for the corrosion of 7075 AA because authors assumed an important effect of the passive layer on the

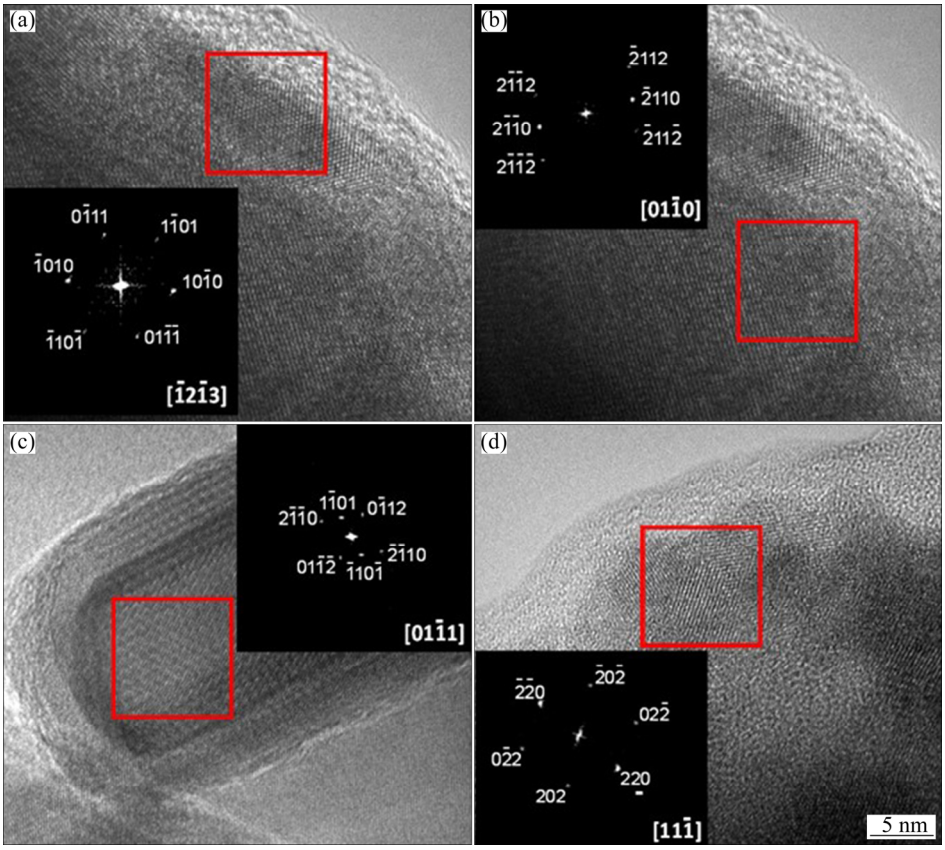

Fig. 10 HAZs of welded samples characterized by HR-TEM and electron diffraction patterns from FFT: (a) $MgZn_2$ precipitate, 0 mT; (b) Al_7Cu_2Fe phase, 0 mT; (c) $MgZn_2$ precipitate, 0 mT; (d) $Al_{18}Cr_2Mg_3$ phase, 12 mT

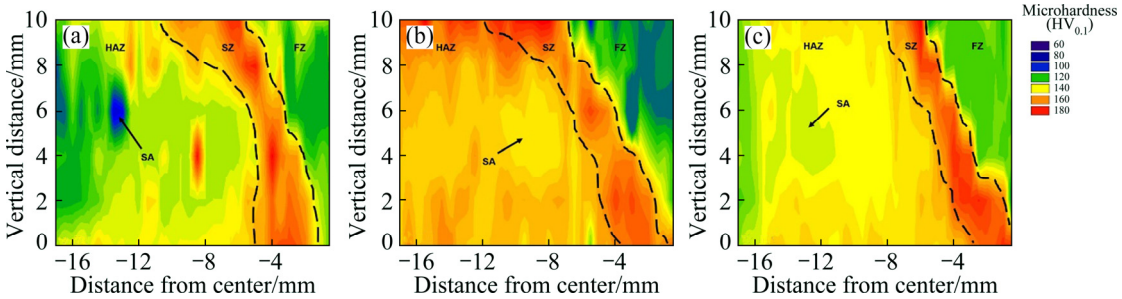

Fig. 11 Microhardness ($HV_{0.1}$) profiles of welds made with different EMILI: (a) 0 mT; (b) 3 mT; (c) 12 mT

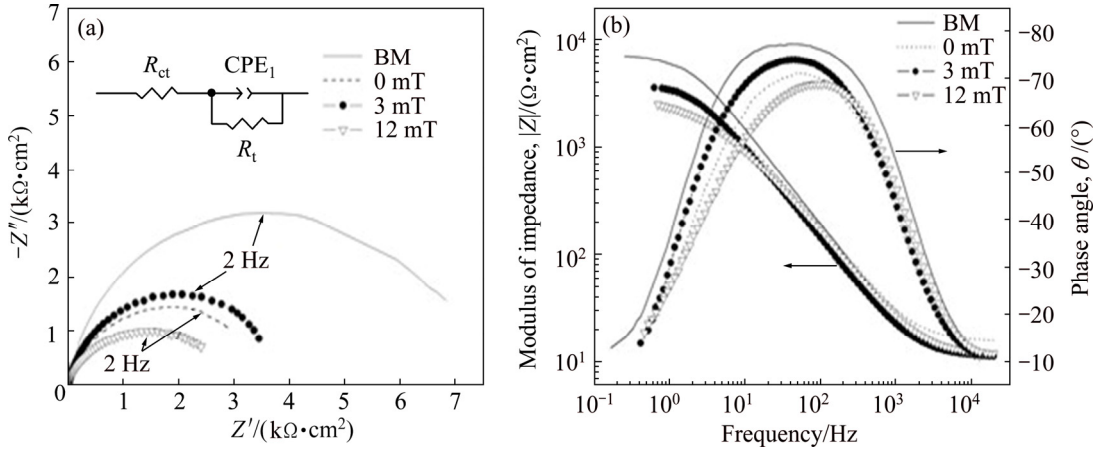

Fig. 12 Nyquist plots (a) and bode plots (b) from EIS measurements performed on 7075-T651 AA samples in natural seawater under different welding conditions

electrochemical behavior of this alloy in borate buffer [27]. However, in the present study, the effect of the passive layer in natural seawater was not observed.

In Fig. 12(a), the equivalent electric circuit was used to analyze the impedance spectra. This equivalent electric circuit represents the mechanism at the interphase controlled by charge transfer. It is important to point out that the proposed equivalent electric circuit must agree with the kinetics of the involved electrochemical reactions. The electric circuit elements, R_{sol}, R_{ct} and CPE are the solution resistance, the charge-transfer resistance and the constant-phase element, respectively. Replacing the capacitor by CPE is a common practice in electrochemical studies and improves the fitting in experimental EIS curves [47]. Capacitors often do not behave ideally in EIS experiments. The double-layer on an electrode surface often behaves like a CPE but not like a capacitor. In real systems, the results obtained from EIS are generally observed as a depressed semicircle in Nyquist plots. This behavior is usually associated with surface roughness, superficial porosity, among others. In order to adjust the Nyquist diagrams with depression in an equivalent electrical circuit, the "constant phase elements" are used. The impedance of CPE (Z_{CPE}) is given by [47,48]:

$$Z_{CPE} = \frac{1}{Y_0}(j\omega)^{-\alpha} \quad (2)$$

where Y_0 is the magnitude, ω is the peak frequency and α is the exponential term (here $0<\alpha<1$, and $\alpha=1$ recovers a perfect capacitor).

Z_{CPE} can provide a description of the behavior of the electrified interphase as it is related to several components with different capacitances on the surface. In many cases, it provides good fit with data from impedance measurements of multiphase alloys and is also suitable to model discontinuities or defects at the atomic scale, as well as microscopic surface roughness [27,49]. In the present case, the CPE parameter was associated to the capacitance behavior of the metal-electrolyte electrified interface.

The R_{ct} values shown in Fig. 13, determined using the Zview software, were 8227, 3394, 3986 and 1504 Ω·cm^2 for base metal, 0, 3 and 12 mT samples, respectively. According to the R_{ct} values, the poorer condition in terms of electrochemical corrosion resistance is for welded sample under the effect of electromagnetic field of 12 mT. The application of EMILI during welding reduces the size of HAZ and also induces the precipitate of the ternary *S*′-phase in FZ. *S*′-phase (Al_2CuMg) nucleates and grows during solidification and cooling of welded metal, starting as a segregated eutectic. This phase with Cu and Mg contents has a negative effect on the passive film formation, stability and homogeneity and consequently on the corrosion resistance of these joints [24,28].

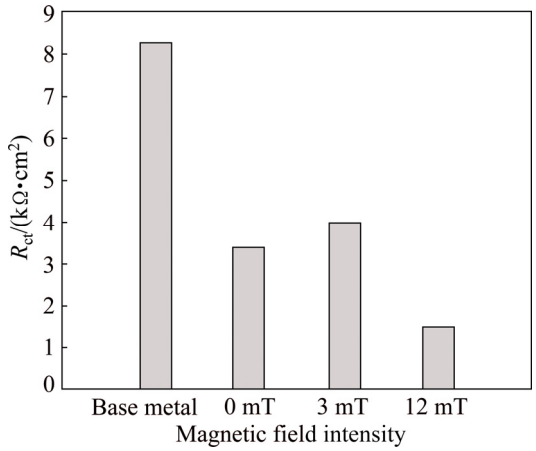

Fig. 13 R_{ct} values from EIS measurements on 7075-T651 AA samples in natural seawater with different welding conditions

ZOLTOWSKI [50] reported that the capacitance estimation from the Y_0 parameter of CPE in depressed semicircles is illogical. WU et al [48] and MA et al [51] demonstrated that for these cases, the capacitance (C) and time constant (τ) can be calculated from Eqs. (3) and (4).

$$C = (Y_0 R^{1-\alpha})^{1/\alpha} \quad (3)$$

$$\tau = \sqrt[\alpha]{Y_0 R} \quad (4)$$

The analysis of the capacitance indicates that the highest value is for samples welded with 12 mT of electromagnetic field and the lowest value is for the BM sample, as shown in Fig. 14. The values of the time constant (τ) that is a parameter indicating the time required for the charging/discharging of the C, are also show in Fig. 14. In the present case, the highest value of τ, and therefore the slower corrosion process, is for BM

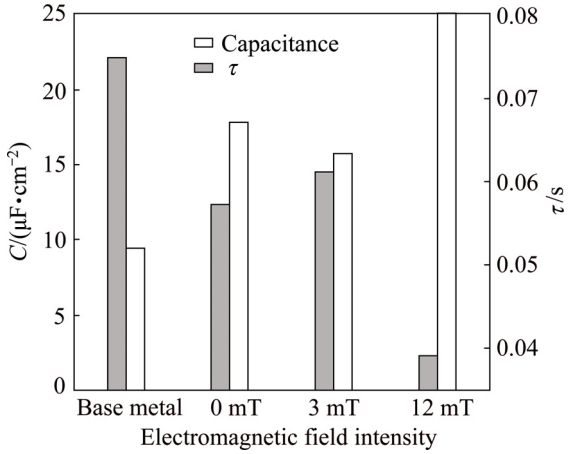

Fig. 14 Capacitance (C) and time constant (τ) values from EIS measurements on 7075-T651 AA samples in natural seawater under different welding conditions

samples, whereas the lowest time constant, faster corrosion process, is for samples welded with 12 mT. This suggests that in the BM a slow corrosion process occurs (lower charge and higher time constant), which translates into a low corrosion rate. The opposite case is observed for the sample welded with 12 mT which presents a fast corrosion process (higher charge and lower time constant), which means a high corrosion rate.

4 Discussion

Figure 5 shows that weld profiles change when EMILI is applied due to the electromagnetic stirring (EMS) of the weld pool which increases the molten BM and reduces the HAZ. This effect is due to the detaching of the partially melted BM into the weld pool as the EMS of the liquid metal increased [39].

However, weld made with 12 mT presents an excess of penetration but weld made with an intensity of 3 mT is acceptable and presents a smaller grain size, as shown in Fig. 6 and the data of cumulative frequency are shown in Fig. 7. The effect on penetration of the weld and the slightly coarsening of the weld microstructure can be correlated with the EMILI during welding, which increases the Lorentz force and downwards in the weld pool. Therefore, an increase of EMILI up to 12 mT appears in the downward direction. This, in turn, produces a descending flow in the weld pool that transfers hot metal to the bottom of the pool, where melt-back of the metal results in a deep pool and a heat sink, which can slow the solidification rate, and mechanism is studied in a parallel work. In addition, the EMS reduced the thermal gradients between the weld pool and adjacent metal, along with the possible reduction of copper precipitation in the segregation zone and a magnetic constriction could be induced by the difference of magnetic susceptibility between the liquid metal of the weld pool and the solid BM.

Cu-rich phases affect negatively the corrosion resistance of AA [24,28,46], and it is well known that the size and distribution of these phases in heat treatable alloys as 7075 AA also affect the mechanical properties of these alloys. The Al_2Cu phase was found in all weld zones at the grain boundaries as eutectic intermetallic compound can be seen in Fig. 8. This finding of Cu-rich phases in weld metal is attributable to the dragging of partial molten BM and the migration phenomena. Nevertheless, XRD patterns in Fig. 9 show an important attenuation of the reflection pecks of the Al_2Cu phase when EMILI of 3 mT is applied during welding. These indicate the possibility of a growth suppression of the Al_2Cu, attributable to the constriction induced by the difference of magnetic susceptibility between the Al matrix and the segregation of copper.

During fusion welding process, the welding thermal cycle promotes the transformation of $\eta' \rightarrow \eta$ in the HAZ in the temperature range of 230 to 350 °C [21−23], and this can reduce the mechanical properties, but EMILI improves the mechanical properties in the HAZ of the welded joints, because the EMILI delays $\eta' \rightarrow \eta$ transformation, as can be seen in Fig. 11, the phenomenon that is now investigated.

The active dissolution of the welded samples in natural seawater can be related with the high density distribution of active precipitates. Nonetheless, the higher corrosion rate of the sample welded without EMILI indicates that copper phases made this alloy very reactive, and when these phases are suppressed an slight improvement can be reached.

From impedance measurements the welded sample with 12 mT presents the lowest R_{ct}, as shown in Fig. 13, this is attributable to the excess of molten base metal dragged into the weld pool and the formation of the ternary S'-phase (Al_2CuMg), promoting a negative effect on the stability and homogeneity of the passive film of AA because the presence of Mg and Cu, but the detrimental effect of the welding process can be reduced when an EMILI of 3 mT is applied.

5 Conclusions

(1) The EMILI of 3 mT in conjunction with the MIEA technique makes an enhancement of micro-structural characteristics and mechanical properties of 7075 AA, thus both can be used as an alternative to improve or diminish the worsening overaging phenomenon in this alloy.

(2) The grain refinement observed in the fusion zone and segregation zone is attributable to the detachment of the parent metal, which in combination with the external electromagnetic stirring induced by the EMILI, increases sites for heterogeneous nucleation, promoting a grain refinement. As a consequence, the mechanical properties of the heat affected zone and the weld pool increase compared with the welded joint without EMILI.

(3) EIS results indicate that the sample welded with 3 mT has an improvement on the corrosion resistance in comparison with the welded sample without EMILI in the weld condition in natural seawater due to the redistribution of reinforcing phases and limitation on the segregation of low melting point elements.

Acknowledgements

J. S. Reyna-Montoya thanks CONACyT-México for providing the scholarship.

References

[1] VASUDEVAN A K, DOHERTY R D. Aluminum alloys — Contemporary research and applications: Contemporary research and applications [M]. Boston: Academic Press, 1989.

[2] LÖFFLER H, KOVÁCS I, LENDVAI J. Decomposition processes in Al−Zn−Mg alloys [J]. Journal of Materials Science, 1983, 18(8): 2215−2240.

[3] ROMETSCH P A, ZHANG Y, KNIGHT S. Heat treatment of 7xxx series aluminium alloys—Some recent developments [J]. Transactions of Nonferrous Metals Society of China, 2014, 24(7): 2003−2017.

[4] MONDOLFO L F. Aluminum alloys: Structure and properties [M]. London: Butterworth & Co. Ltd., 1979.

[5] YANG Rong-xian, LIU Zhi-yi, YING Pu-you, LI Jun-lin, LIN Liang-hua, ZENG Su-min. Multistage-aging process effect on formation of GP zones and mechanical properties in Al−Zn−Mg−Cu alloy [J]. Transactions of Nonferrous Metals Society of China, 2016, 26(5): 1183−1190.

[6] ÇAM G, İPEKOĞLU G. Recent developments in joining of aluminum alloys [J]. The International Journal of Advanced Manufacturing Technology, 2017, 91(5): 1851−1866.

[7] TALBOT D E J. Effects of hydrogen in aluminium, magnesium, copper, and their alloys [J]. International Metallurgical Reviews, 1975, 20(1): 166−184.

[8] LIN R Y, HOCH M. The solubility of hydrogen in molten aluminum alloys [J]. Metallurgical Transactions A, 1989, 20(9): 1785−1791.

[9] WU S C, YU X, ZUO R Z, ZHANG W H, XIE H L, JIANG J Z. Porosity, element loss, and strength model on softening behavior of hybrid laser arc welded Al−Zn−Mg−Cu alloy with synchrotron radiation analysis [J]. Welding Journal, 2013, 92: 64−71.

[10] WU S C, YU C, ZHANG W H, FU Y N, HELFEN L. Porosity induced fatigue damage of laser welded 7075-T6 joints investigated via synchrotron X-ray microtomography [J]. Science and Technology of Welding and Joining, 2015, 20(1): 11−19.

[11] LI Kai, LU Feng-gui, GUO Song-tao, CUI Hai-chao, TANG Xin-hua. Porosity sensitivity of A356 Al alloy during fiber laser welding [J]. Transactions of Nonferrous Metals Society of China, 2015, 25(8): 2516−2523.

[12] LI Quan, WU Ai-ping, LI Yan-jun, WANG Guo-qing, QI Bo-jin, YAN Dong-yang, XIONG Lin-yu. Segregation in fusion weld of 2219 aluminum alloy and its influence on mechanical properties of weld [J]. Transactions of Nonferrous Metals Society of China, 2017, 27(2): 258−271.

[13] CHENG C M, CHOU C P, LEE I K, LIN H Y. Hot cracking of welds on heat treatable aluminium alloys [J]. Science and Technology of Welding and Joining, 2005, 10(3): 344−352.

[14] KOU S. Solidification and liquation cracking issues in welding [J]. JOM, 2003, 55(6): 37−42.

[15] CHANG C C. Microstructure in hot cracking mechanism of welded aluminium alloys [J]. Materials Science and Technology, 2013, 29(4): 504−510.

[16] ASHTON R F, WESLEY R P, DIXON C R. The effect of porosity on 5086-H116 aluminum alloy welds [J]. Welding Journal, 1975, 54(3): 96−98.

[17] RUDY J F, RUPERT E J. Effects of porosity on mechanical properties of aluminum welds [J]. Welding Journal, 1970, 49(7): 322−336.

[18] HUANG C, KOU S. Partially melted zone in aluminum welds—Solute segregation and mechanical behavior [J]. Welding Journal, 2001, 80(1): 9−17.

[19] HUANG C, KOU S. Partially melted zone in Aluminum welds-liquation mechanism and directional soldification [J]. Welding Journal, 2000, 79(5): 113−120.

[20] JIANG Fu-lin, ZHANG Hui, WENG Shu-chu, FU Ding-fa. Characterization of dynamic microstructural evolution of AA7150 aluminum alloy at high strain rate during hot deformation [J]. Transactions of Nonferrous Metals Society of China, 2016, 26(1): 51−62.

[21] MA T, OUDEN G D. Softening behaviour of Al−Zn−Mg alloys due to welding [J]. Materials Science and Engineering A, 1999, 266(1−2): 198−204.

[22] FU G, TIAN F, WANG H. Studies on softening of heat-affected zone of pulsed-current GMA welded Al−Zn−Mg alloy [J]. Journal of Materials Processing Technology, 2006, 180(1): 216−220.

[23] HWANG R Y, CHOU C P. The study on microstructural and mechanical properties of weld heat affected zone of 7075-T651 aluminum alloy [J]. Scripta Materialia, 1997, 38(2): 215−221.

[24] DONATUS U, THOMPSON G E, OMOTOYINBO J A, ALANEME K K, ARIBO S, AGBABIAKA O G. Corrosion pathways in aluminium alloys [J]. Transactions of Nonferrous Metals Society of China, 2017, 27(1): 55−62.

[25] ELABAR D, NĚMCOVÁ A, HASHIMOTO T, SKELDON P, THOMPSON G E. Effect of sulphate impurity in chromic acid anodizing of aluminium [J]. Corrosion Science, 2015, 100: 377−385.

[26] MIRHASHEMIHAGHIGHI S, ŚWIATOWSKA J, SEYEUX V M A, SALMI S Z E, RITALA M, MARCUS P. Corrosion protection of aluminium by ultra-thin atomic layer deposited alumina coatings [J]. Corrosion Science, 2016, 106: 16−24.

[27] DENG Ying, YE Rui, XU Guo-fu, YANG Ji-dong, PAN Qing-lin, PENG Bing, CAO Xiao-wu, DUAN Yu-lu, WANG Ying-jun, LU Li-ying, YIN Zhi-min. Corrosion behaviour and mechanism of new aerospace Al−Zn−Mg alloy friction stir welded joints and the effects of secondary $Al_3Sc_xZr_{1-x}$ nanoparticles [J]. Corrosion Science, 2015, 90: 359−374.

[28] UMAMAHESHWER R A C, VASU V, GOVINDARAJU M, SRINADH K V S. Stress corrosion cracking behaviour of 7xxx aluminum alloys: A literature review [J]. Transactions of Nonferrous Metals Society of China, 2016, 26(6): 1447−1471.

[29] SZKLARSKA-SMIALOWSKA Z. Pitting corrosion of aluminum [J]. Corrosion Science, 1999, 41(9): 1743−1767.

[30] MCCAFFERTY E. Sequence of steps in the pitting of aluminum by chloride ions [J]. Corrosion Science, 2003, 45(7): 1421−1438.

[31] LI Jin-feng, PENG Zhuo-wei, LI Chao-xing, JIA Zhi-qiang, CHEN Wen-jing, ZHENG Zi-qiao. Mechanical properties, corrosion behaviors and microstructures of 7075 aluminium alloy with various aging treatments [J]. Transactions of Nonferrous Metals Society of China, 2008,18(4): 755−762.

[32] YAN Shao-hua, CHEN Hui, MA Chuan-ping, NIE Yuan, WANG Xiao-min, QIN Qing. Local corrosion behaviour of hybrid laser-MIG welded Al−Zn−Mg alloy joints [J]. Materials & Design, 2015, 88: 1353−1365.

[33] SRINIVASA R K, PRASAD R K. Pitting corrosion of heat-treatable aluminium alloys and welds: A review [J]. Transactions of the Indian Institute of Metals, 2004, 57(6): 593−610.

[34] KUMAR P V, REDDY G M, SRINIVASA R K. Microstructure, mechanical and corrosion behavior of high strength AA7075 aluminium alloy friction stir welds–Effect of post weld heat treatment [J]. Defence Technology, 2015, 11(4): 362−369.

[35] ÇAM G, KOÇAK M. Microstructural and mechanical characterization of electron beam welded Al-alloy 7020 [J]. Journal of Materials Science, 2007, 42(17): 7154−7161.

[36] ÇAM G, MISTIKOGLU S. Recent developments in friction stir welding of Al-alloys [J]. Journal of Materials Engineering and Performance, 2014, 23(6): 1936−1953.

[37] WAHID M A, KHAN Z A, SIDDIQUEE A N. Review on underwater friction stir welding: A variant of friction stir welding with great potential of improving joint properties [J]. Transactions of Nonferrous Metals Society of China, 2018, 28(2): 193−219.

[38] AMBRIZ R R, BARRERA G, GARCÍA R, LÓPEZ V H. A comparative study of the mechanical properties of 6061-T6 GMA welds obtained by the indirect electric arc (IEA) and the modified indirect electric arc (MIEA) [J]. Materials & Design, 2009, 30(7): 2446−2453.

[39] MOUSAVI M G, HERMANS M J M, RICHARDSON I M, DEN-OUDEN G. Grain refinement due to grain detachment in electromagnetically stirred AA7020 welds [J]. Science and Technology of Welding and Joining, 2003, 8(4): 309−312.

[40] SUNDARESAN S, RAM G D JANAKI, MURUGESAN R, VISWANATHAN N. Combined effect of inoculation and magnetic arc oscillation on microstructure and tensile behaviour of type 2090 Al−Li alloy weld fusion zones [J]. Science and Technology of Welding and Joining, 2013, 18(4): 257−264.

[41] GARCÍA-R M A, LÓPEZ-M V H, GARCÍA-H R, CURIEL F F, AMBRÍZ R R. Preliminary assessment of the effects of the application of an axial magnetic field during GMA welding of Al-6063-T6[C]// Structural and Chemical Characterization of Metals, Alloys and Compounds. Warrendale, PA: Materials Research Society 2010: 99−106.

[42] CHEN Rong, WANG Chun-ming, JIANG Ping, SHAO Xin-yu, ZHAO Ze-yang, GAO Zhong-mei, YUE Chen. Effect of axial magnetic field in the laser beam welding of stainless steel to aluminum alloy [J]. Materials & Design, 2016, 109: 146−152.

[43] LIU Y B, SUN Q J, WANG H, ZHANG H M, CAI S J, FENG J C. Effect of the axial external magnetic field on copper/aluminium arc weld joining [J]. Science and Technology of Welding and Joining, 2016, 21(6): 460−465.

[44] LIU Yi-bo, SUN Qing-jie, LIU Jin-ping, WANG Shi-jie, FENG Ji-cai. Effect of axial external magnetic field on cold metal transfer welds of aluminum alloy and stainless steel [J]. Materials Letters, 2015, 152: 29−31.

[45] LIPPOLD J C. Welding metallurgy and weldability [M]. New Jersey, USA: John Wiley & Sons, Inc, 2014.

[46] DAVIS J R. Corrosion of aluminum and aluminum alloys [M]. Materials Park, Novelty: ASM International, 1999.

[47] LASIA A. Electrochemical impedance spectroscopy and its applications [M]. Boston, MA: Springer, 2002.

[48] WU Xiao-juan, MA Hou-yi, CHEN Shen-hao, XU Zhi-yuan, SUI Ai-fen. General equivalent circuits for faradaic electrode processes under electrochemical reaction control [J]. Journal of Electrochemical Society, 1999, 146(5): 1847−1853.

[49] PAJKOSSY T. Impedance of rough capacitive electrodes [J]. Journal of Electroanalytical Chemistry, 1994, 364(1−2): 111−125.

[50] ZOLTOWSKI P. On the electrical capacitance of interfaces exhibiting constant phase element behaviour [J]. Journal of Electroanalytical Chemistry, 1998, 443(1): 149−154.

[51] MA Hou-yi, CHENG Xiao-liang, LI Gui-qiu, CHEN Shen-hao, QUAN Zhen-lan, ZHAO Shi-yong, NIU Lin. The influence of hydrogen sulfide on corrosion of iron under different conditions [J]. Corrosion Science, 2000, 42(10): 1669−1683.

改进间接电弧焊过程中电磁交互作用对7075铝合金显微组织和耐腐蚀性能的影响

J. S. REYNA-MONTOYA[1], M. A. GARCÍA-RENTERÍA[1], V. L. CRUZ-HERNÁNDEZ[2], F. F. CURIEL-LÓPEZ[1], L. R. DZIB-PÉREZ[3], L. A. FALCÓN-FRANCO[1]

1. Faculty of Metallurgy, Autonomous University of Coahuila, Carretera 57 Km. 5 CP 25720, Monclova, Coahuila, México;
2. Instituto de Investigación en Metalurgia y Materiales, Universidad Michoacana de San Nicolás de Hidalgo, A. P. 888, CP 58030, Morelia, Michoacán, México;
3. Centre for Corrosion Research, Autonomous University of Campeche, Av. Agustín Melgar s/n, Col. Buenavista, CP 24039, Campeche, Cam, México

摘　要：研究低强度电磁交互作用(EMILI)对改进间接电弧(MIEA)焊 7075-T651 铝合金板(厚度为 13 mm)的显微组织和耐腐蚀性能的影响。焊接过程为单道次，热输入约为 1.5 kJ/mm。通过测量显微硬度和电化学阻抗谱分别研究 EMILI 对局部力学性能和天然海水中耐蚀性的影响，并将其与焊缝的显微组织观察结果相关联。焊缝的显微组织表征表明，在电磁搅拌作用下，3 mT 的 EMILI 使焊缝金属的晶粒细化。此外，扫描电镜观察表明，热影响区(HAZ)的富铜相析出和共晶偏析也因受到 EMILI 的影响而减少。使用 3 mT 的 EMILI 焊接可以减少 7075-T651 焊缝在天然海水中的腐蚀溶解性和热影响区的过时效程度。因此，EMILI 结合 MIEA 技术可使焊接接头具有更好的显微组织特征，能改善热影响区的力学性能，降低电化学活性。

关键词：7075-T651 铝合金；改进间接电弧焊；显微组织表征；耐腐蚀性；电磁交互作用

(Edited by Wei-ping CHEN)